Supplement of The Cryosphere, 19, 1373–1390, 2025
https://doi.org/10.5194/tc-19-1373-2025-supplement

The Cryosphere Open Access EGU

Supplement of

What does the impurity variability at the microscale represent in ice cores? Insights from a conceptual approach

Piers Larkman et al.

Correspondence to: Piers Larkman (piersmichael.larkman@unive.it)

S1 Expansion to empirical and modelled results

Intensity values are not directly comparable between LA-ICP-MS measurements as data is un-calibrated. Drops to zero intensity represent regions where impurity content was below limits of detection.

Plots for EDC LGP

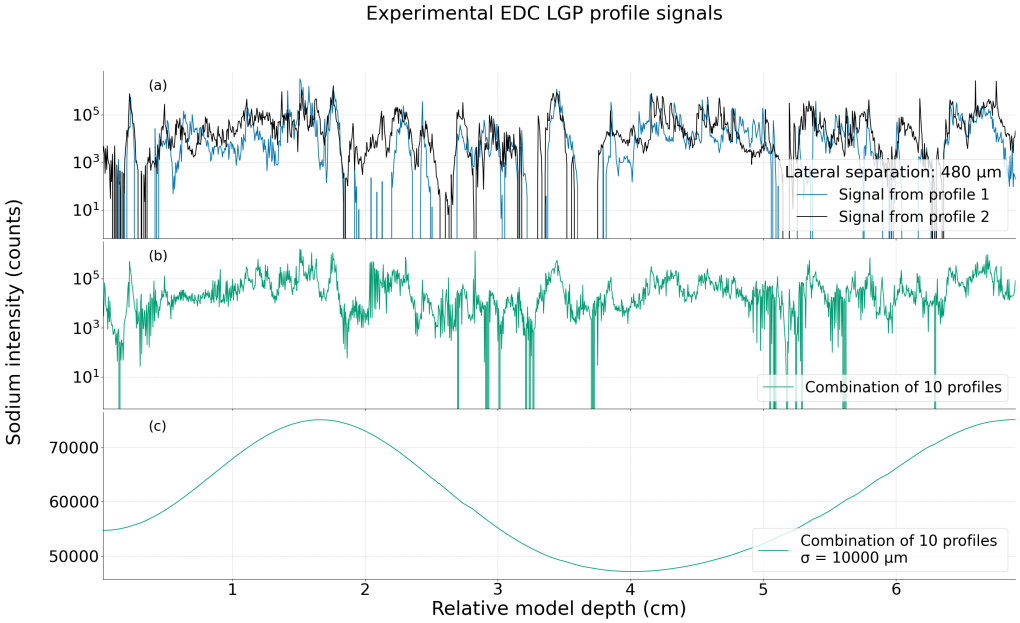

Figure S1. Measured LA-ICP-MS signals from line profiles taken across the surface of the EDC LGP sample. All profiles run down the central core axis. Panel (a) shows two signals resulting from two parallel laser tracks. Panel (b) shows the spatially averaged signal resulting from combining all measured parallel profiles, including the two signals in (a), with a range of lateral separations between adjacent profiles. Panel (c) shows this spatially averaged signal after smoothing to a CFA-like resolution of 1 cm.

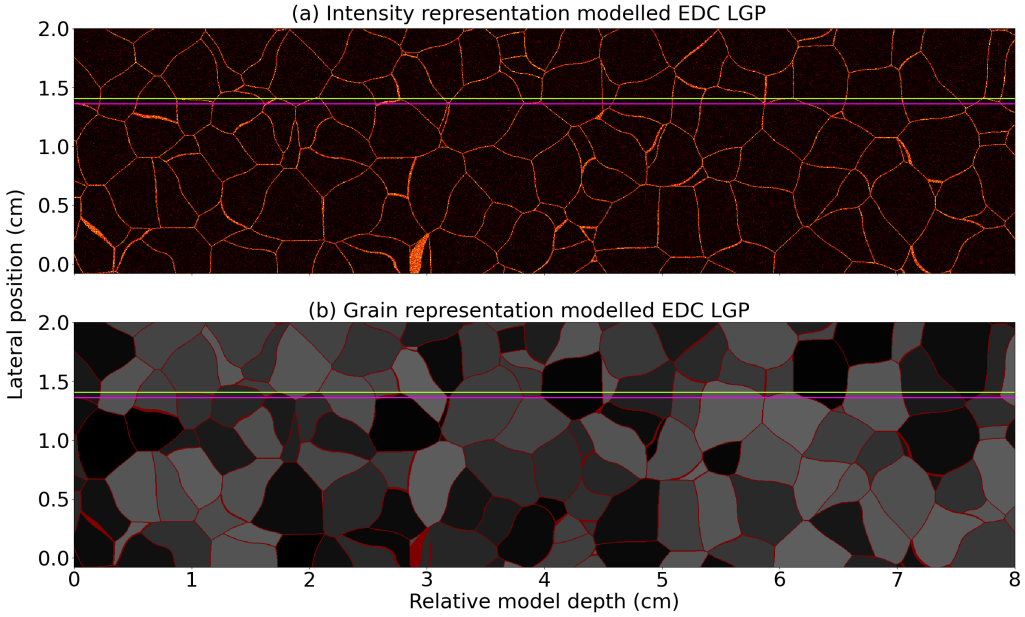

Figure S2. The intensity, (a), and structural, (b), representations of one modelled face of the EDC LGP sample. The structural representation shows grains as different colours, separated by grain boundaries represented in black. Each of the rows in the intensity representation can be taken as a separate laser profile. The green and magenta lines in both panels show the track of the profiles plotted in Fig. S3.

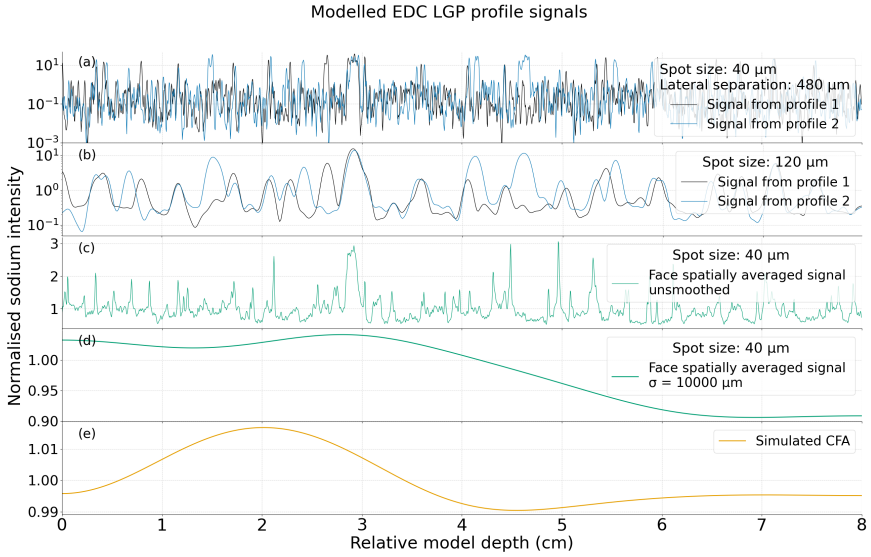

Figure S3. Line profile signals for the modelled EDC Holocene ice with intensity normalised by dividing the signal by the volume average intensity. Panel (a) shows signals acquired from 40 μm spot size profiles taken from the tracks indicated in Fig. S2. Signals resulting from simulating a 120 μm spot size along these profiles are shown in (b). The resulting signal from combining all possible profiles from the face in Fig. S2 is shown unsmoothed in (c) and smoothed to CFA resolution in (d). The simulated CFA signal is plotted in (e). Note the different y-axis scales for each panel.

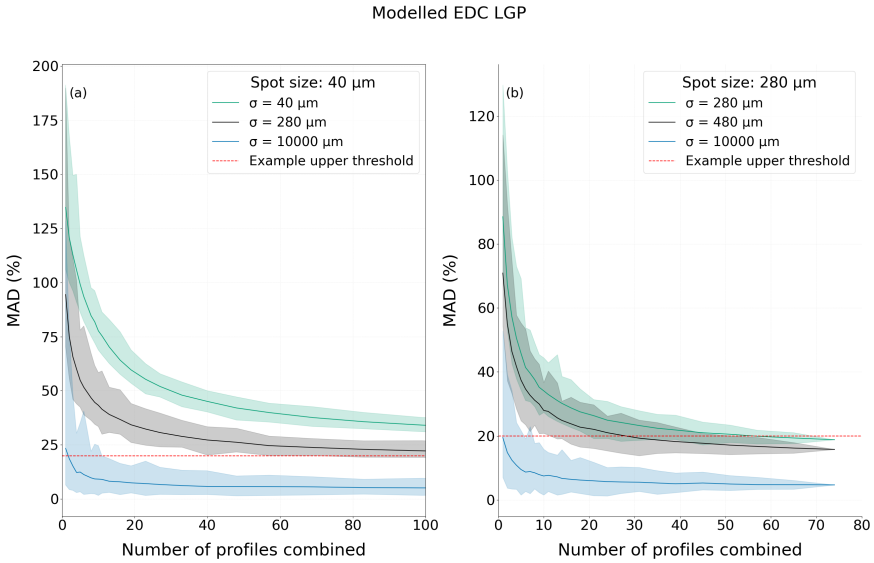

Figure S4. Plots of calculated MAD values against the number of LA-ICP-MS profiles used to construct a spatially averaged signal for the modelled EDC LGP face shown in Fig. S2. As there are multiple ways to choose profiles for combination into a spatially averaged signal, the solid line of each colour shows the mean result and the shaded region shows the range of MADs acquired for different possible profile combinations. Panel (a) shows results from simulating a 40 μm laser spot and (b) a 280 μm laser spot. Different coloured regions show MAD values resulting from smoothing signals with different width Gaussian kernels. An arbitrary threshold of 20 % is also shown (red line).

Plots for RECAP Holocene

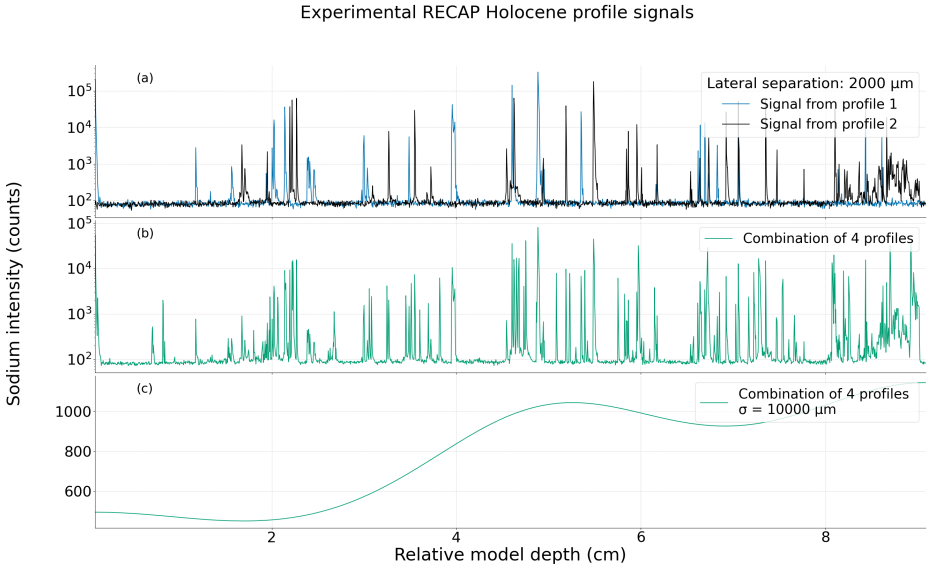

Figure S5. Plots equivalent to Fig. S1 showing the experimentally measured profiles from the RECAP Holocene sample.

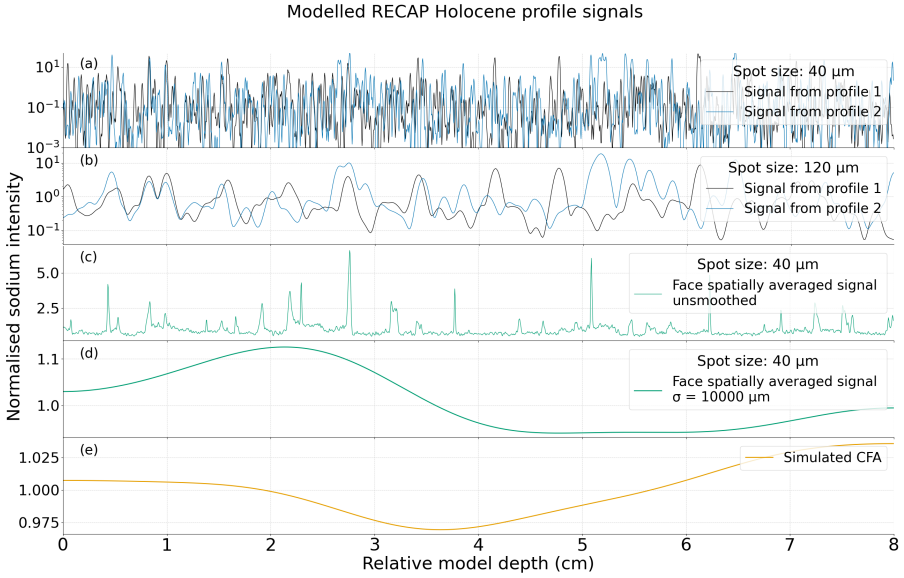

Figure S6. Plots equivalent to Fig. S3 for the modelled RECAP Holocene sample.

Plots for RECAP LGP

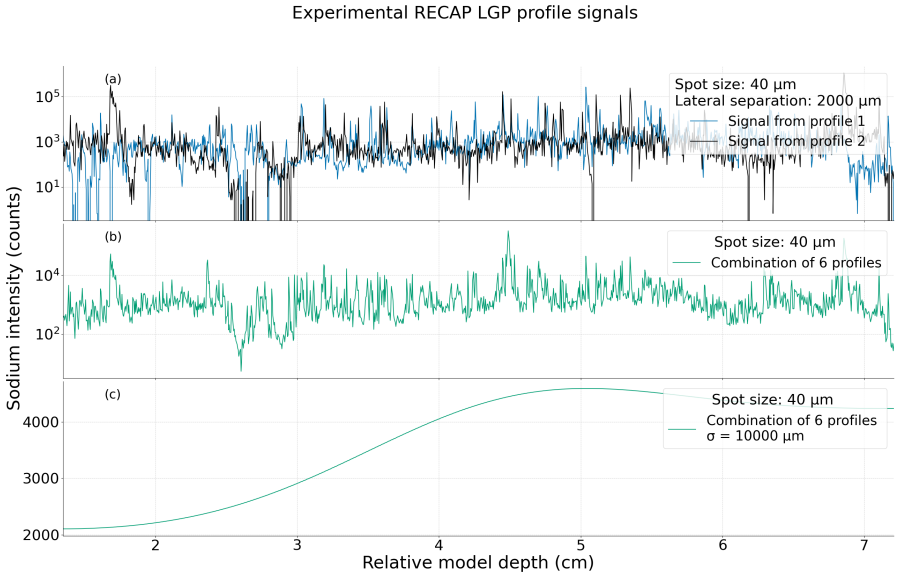

Figure S7. Plots equivalent to Fig. S1 showing the modelled data for the RECAP LGP sample.

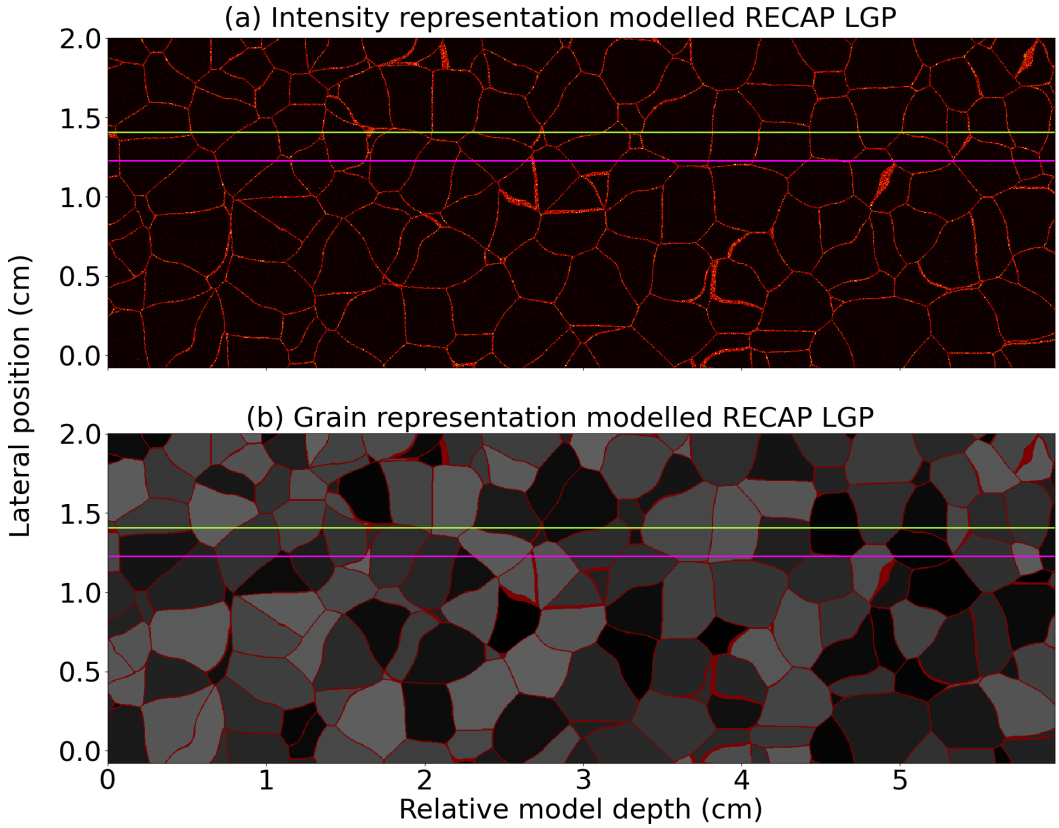

Figure S8. Plots equivalent to Fig. S2 showing the modelled data for the RECAP LGP sample.

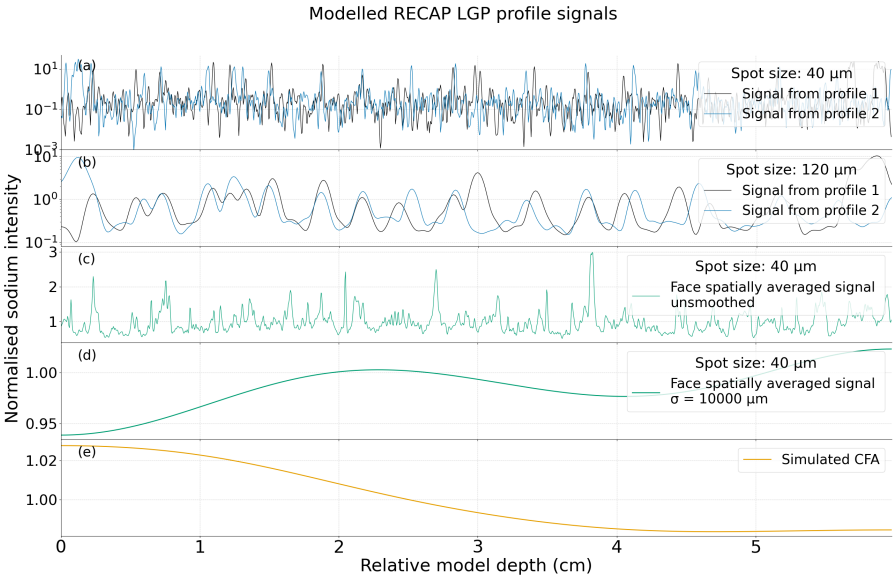

Figure S9. Plots equivalent to Fig. S3 showing the two profiles plotted in Fig. S8 for modelled the RECAP LGP sample.

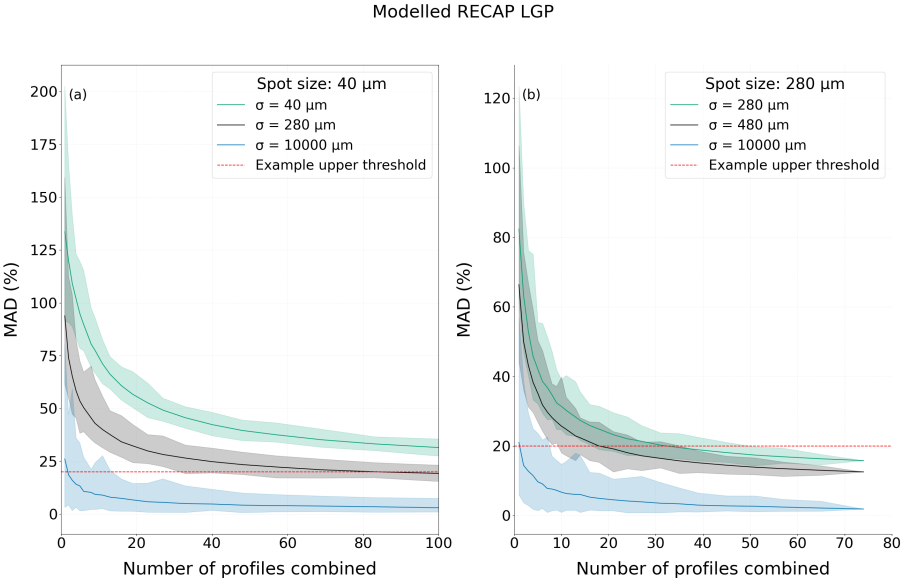

Figure S10. Plots equivalent to Fig. S4 for the modelled RECAP LGM sample.

S2 Modelled grain volumes

The three-dimensional Poisson Voronoi tessellations used for this analysis are parameterised by the grain number density that matches the ice samples they represent. This number density, n, is calculated in a specific ice sample as

$$n = \frac{1}{\frac{4}{3}\pi\bar{r}^3} \tag{S1}$$

for a sample with grains of mean radius $\bar{r}$, assuming spherical grain volume. The grain number density from equation S1 can be multiplied by the total volume of a modelled space, V,

$$N = Vn \tag{S2}$$

to get the total number of seed points, N, required to produce grains with mean size matching the target ice samples. Generating a Poisson Voronoi tessellation with a number of seeds set by equation S2 results in a modelled space that contains grains of varying volumes, v_i, with a mean grain volume $\bar{v}$,

$$\bar{v} = \frac{1}{N}\sum_{i=1}^{N} v_i. \tag{S3}$$

From this mean grain volume, a normalised grain volume y can be defined as

$$y = \frac{v}{\bar{v}}. \tag{S4}$$

Grains vary in size conforming to a gamma distribution (Ferenc and Néda, 2007)

$$f(y) = \frac{3125}{24}(y)^4 \exp(-5y) \tag{S5}$$

which is plotted in figures S11, S13, and S14 alongside observed modelled grain size distributions.

Fig. S11 shows that modelled systems' grain volumes match the theoretical gamma distribution, with a shift to slightly smaller grain volumes than targetted, and a large number of grains with very small volumes. This change in distribution can be explained by considering that, for all ice samples presented in this study, the ratio of the mean grain radius to the modelled volume size results in grains that only exist partially within the modelled space. Typically, grain size analysis will be carried out only considering the Voronoi cells (grains) that are wholly contained in the modelled volume (Quey et al., 2011). Therefore, to truly extract the grain volume distribution, a sufficient number of grains must exist wholly within the simulated volume, which is not the case for samples modelled in this study.

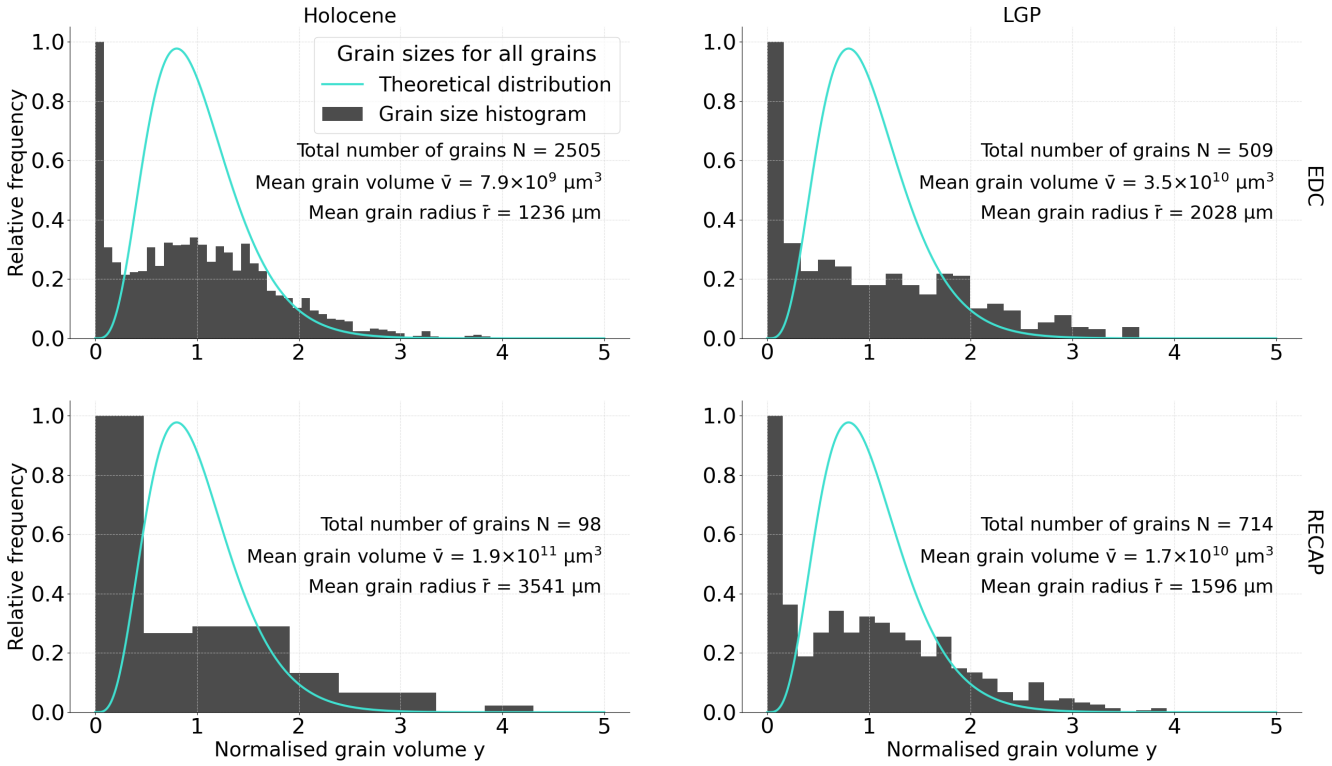

Figure S11. Grain volume distribution for all modelled samples. Bin widths differ due to the different total numbers of grains.

To explore the statistics of grain volumes generated by the Voronoi tessellation used in this study, a model which has a large number of grains wholly within its volume was produced. This modelled volume, shown partially in Fig. S12, has a relatively large cubic volume, with voxel dimension $40\,\mu\mathrm{m}$, volume side length $12000\,\mu\mathrm{m}$, and a relatively small target grain radius of $400\,\mu\mathrm{m}$. This modelled volume does not represent any specific physical ice sample. Figure S13 shows the grain volume distribution for all grains in this space, calculated by counting the number of voxels in each grain. Figure S14 shows the subset of grains, only 15% of the total, in this volume that are wholly contained. The grains contained wholly in the volume have an average grain radius of $410\,\mu\mathrm{m}$ and conform well to the expected grain volume distribution reported in equation S5.

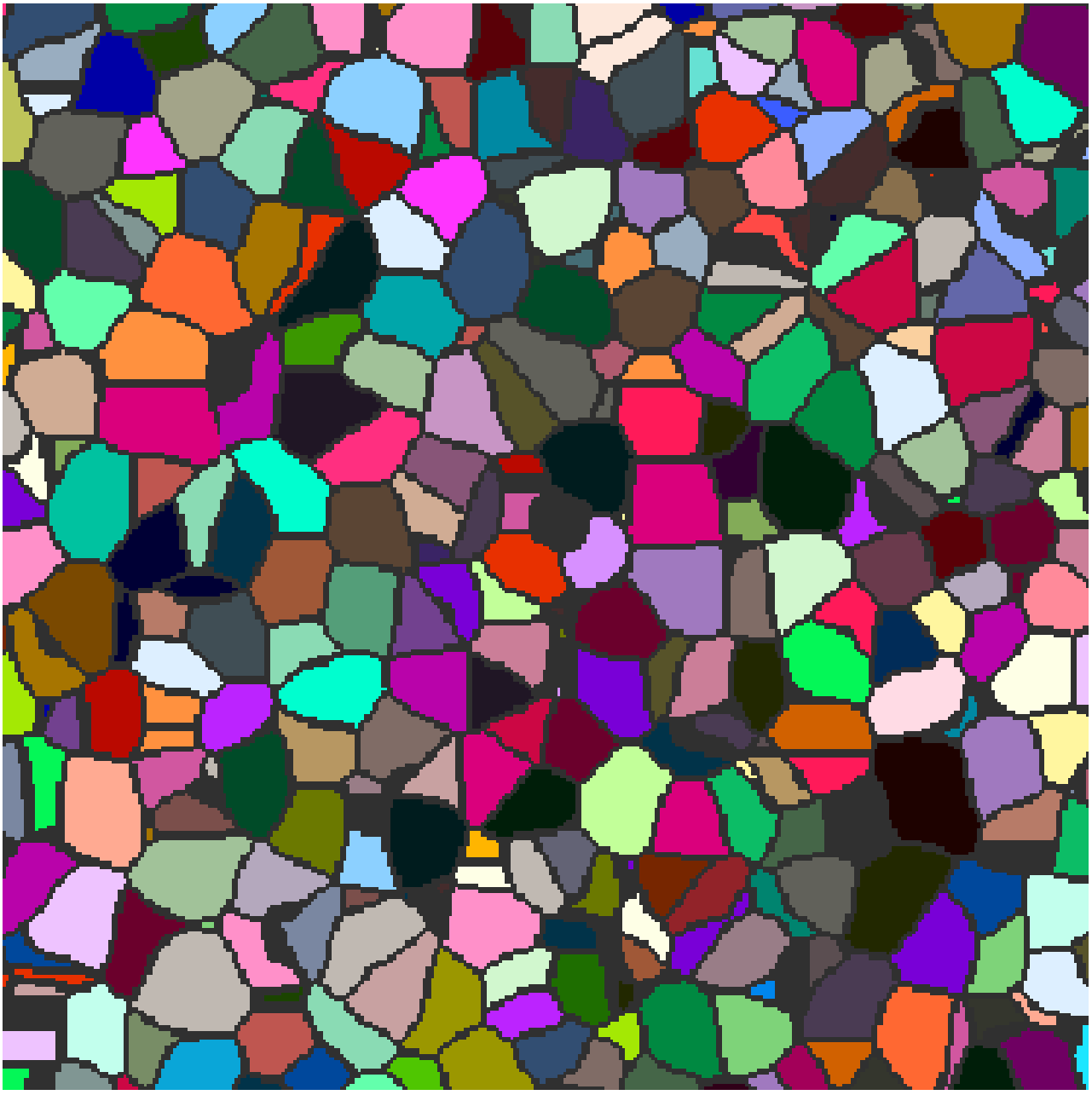

Figure S12. Two-dimensional representation of a face of a cube, dimension 12 000 µm, with grains resulting from a Poisson Voronoi tessellation shown in different colours and the boundaries between these grains shown in grey.

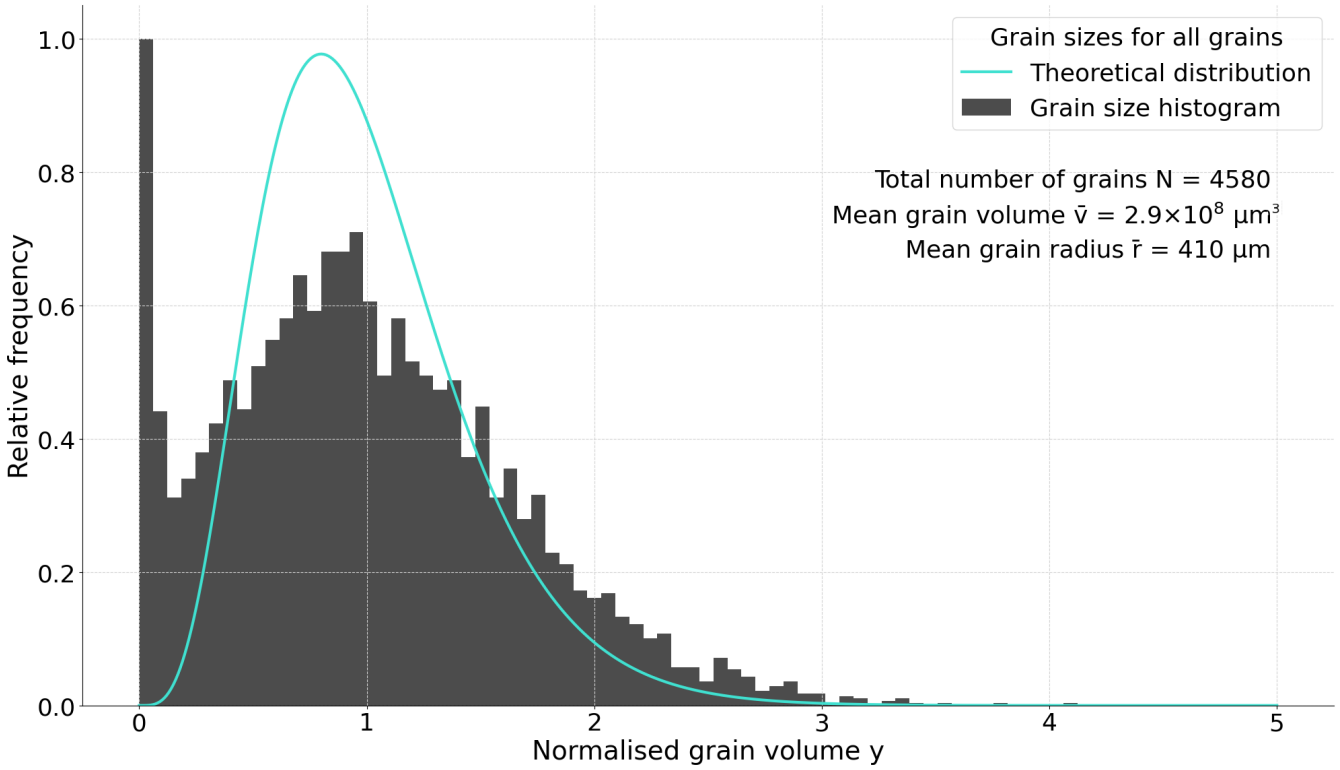

Figure S13. Grain volume distribution for all grains generated in Fig. S12.

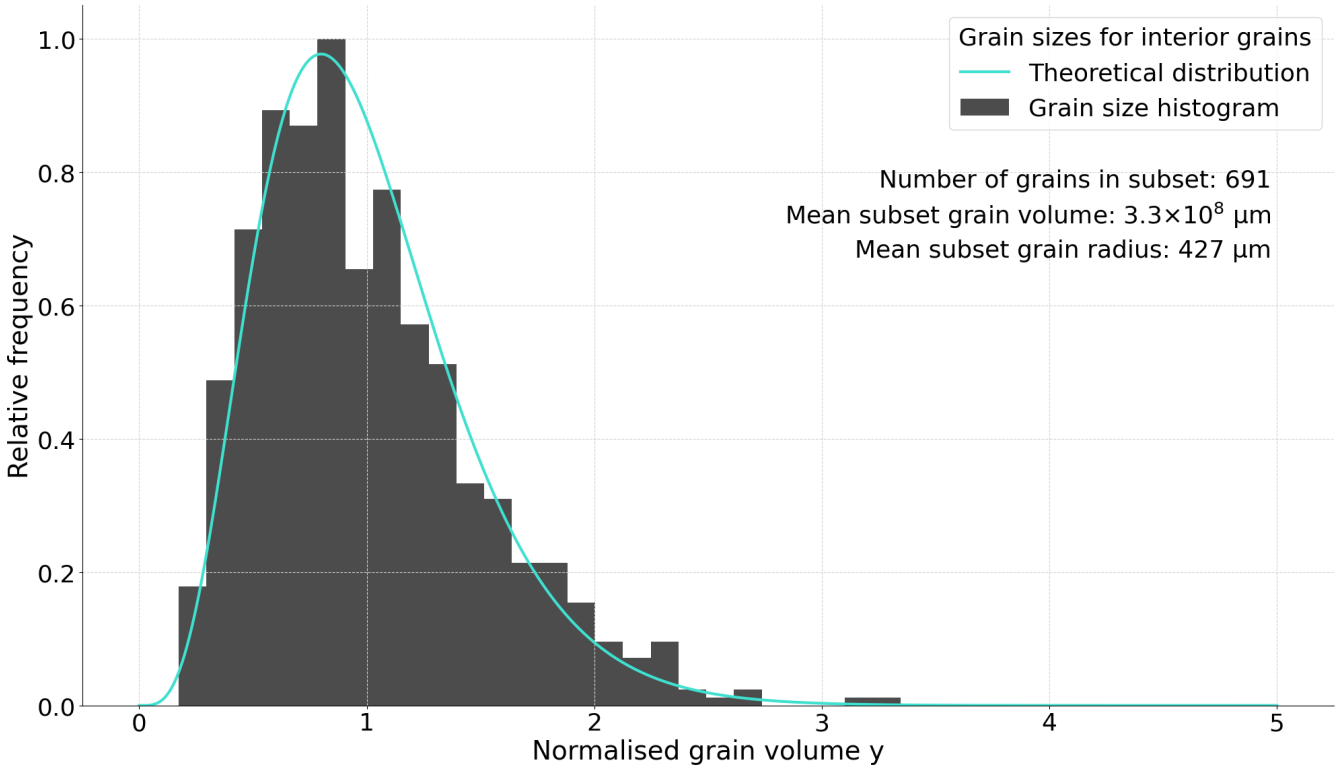

Figure S14. Grain volume distribution for the subset of grains fully contained within the same space as data plotted in Fig. S13.

Verification that modelled ice samples have a suitable grain volume distribution therefore can come from comparison with figures S13 and S14. To further verify these distributions, techniques such as that used for analysing high-resolution microstructure data (Binder et al., 2013) could also be applied to estimate grain volumes.

S3 Calibrated data results

EDC Holocene

Figures for data modelled from calibrated LA-ICP-MS images taken from a section of EDC ice at a depth of 281.8 m, published by Bohleber et al. (2024).

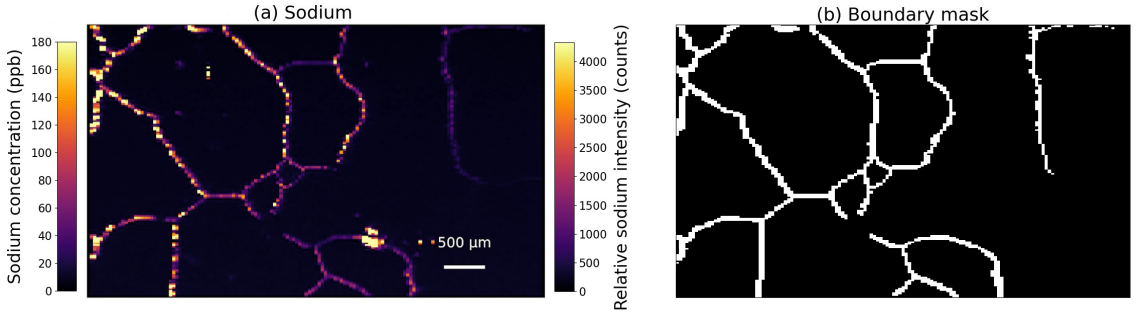

Figure S15. Measured laser ablation inductively coupled plasma mass spectrometry (LA-ICP-MS) data with both calibrated and uncalibrated scales (a) and segmentation mask (b) showing the input data used to model calibrated EDC Holocene ice.

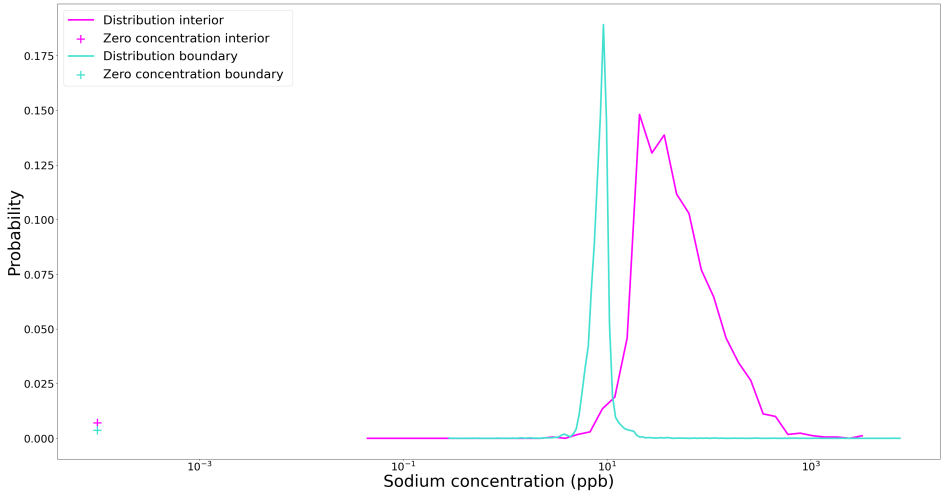

Figure S16. The probability distributions for the likelihood of a model voxel being assigned a certain concentration for boundary and interior voxels, according to the data shown in Fig. S20.

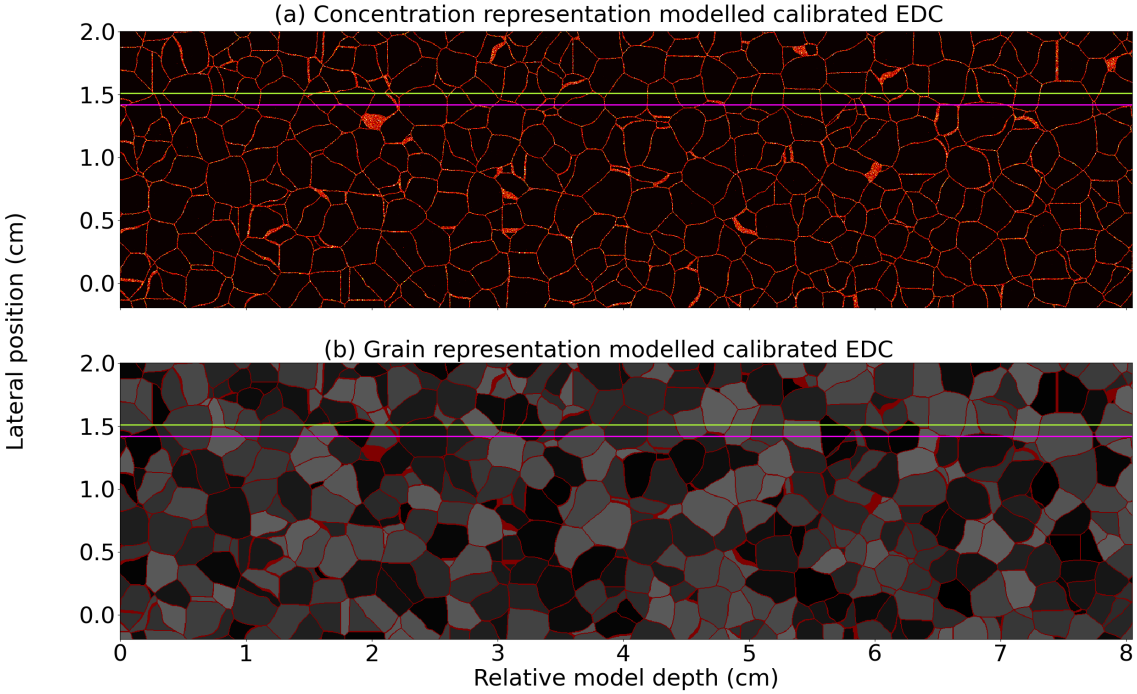

Figure S17. Plots equivalent to Fig. S2 showing the modelled data for the calibrated EDC Holocene dataset.

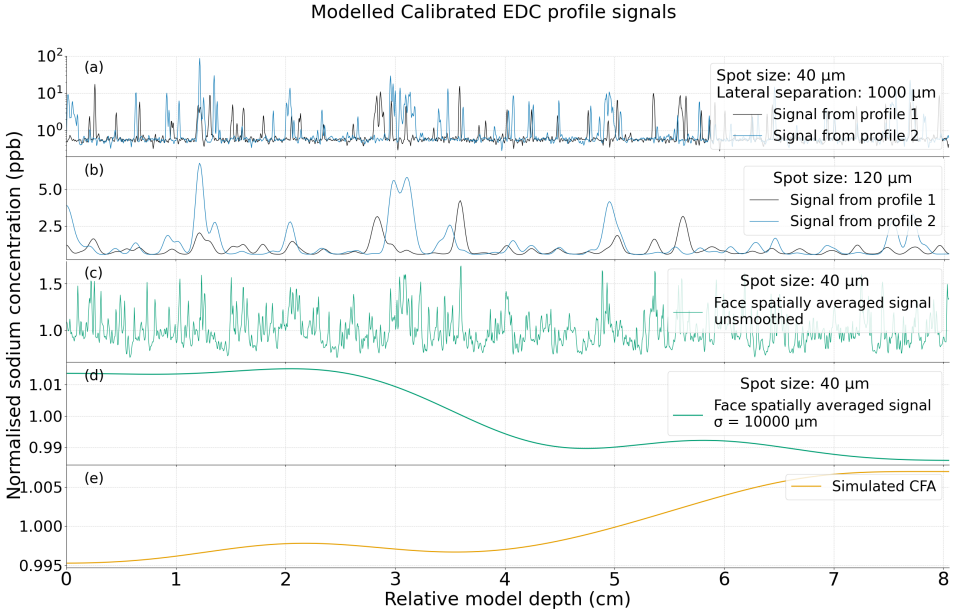

Figure S18. Plots equivalent to Fig. S3 showing the two profiles plotted in Fig. S22 for modelled calibrated EDC Holocene data.

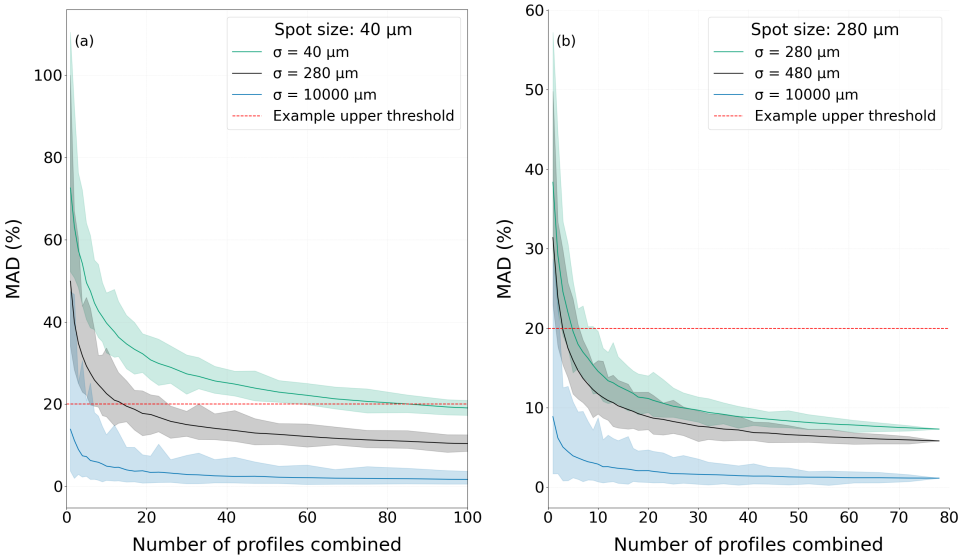

Figure S19. Plots equivalent to Fig. S4 for modelled calibrated EDC Holocene data.

EDC LGP

Figures for data modelled from calibrated LA-ICP-MS images taken from a section of EDC ice at a depth of 1,096.5 m, published by Bohleber et al. (2024).

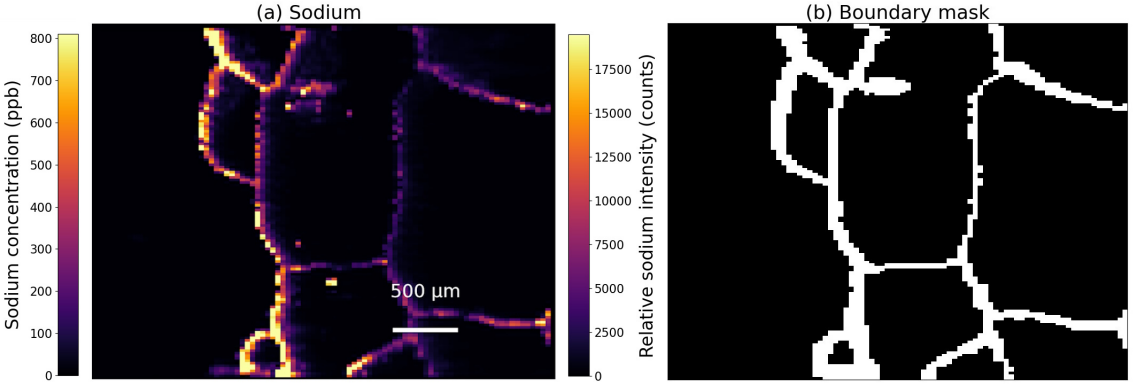

Figure S20. Measured LA-ICP-MS data with both calibrated and uncalibrated scales (a) and segmentation mask (b) showing the input data used to model calibrated EDC LGP ice.

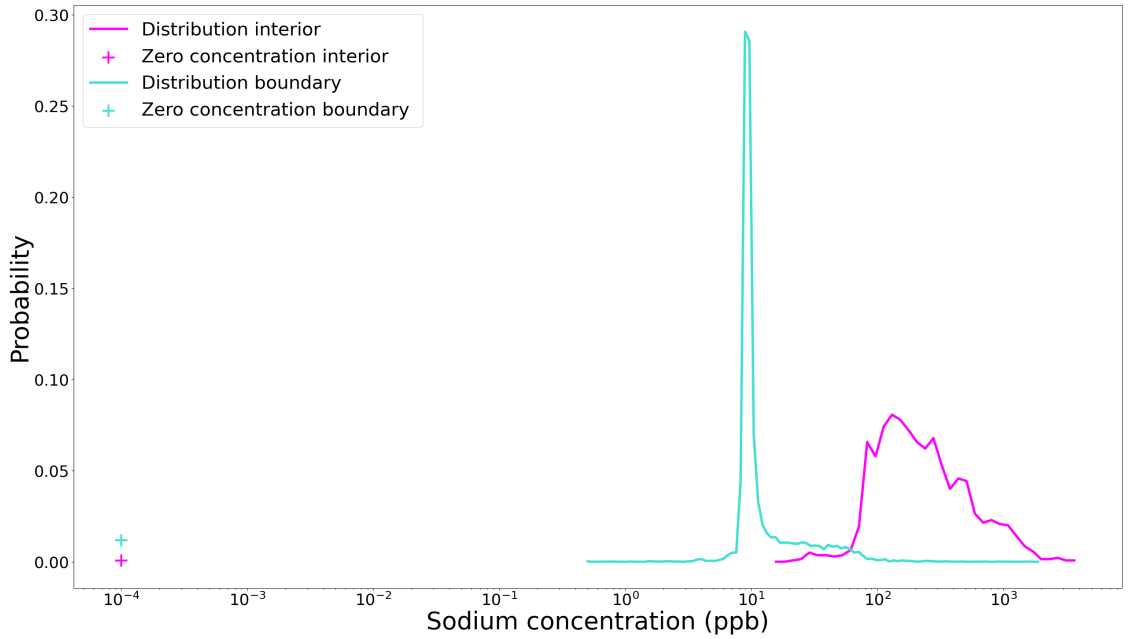

Figure S21. The probability distributions for the likelihood of a model voxel being assigned a certain concentration for boundary and interior voxels, according to the data shown in Fig. S20.

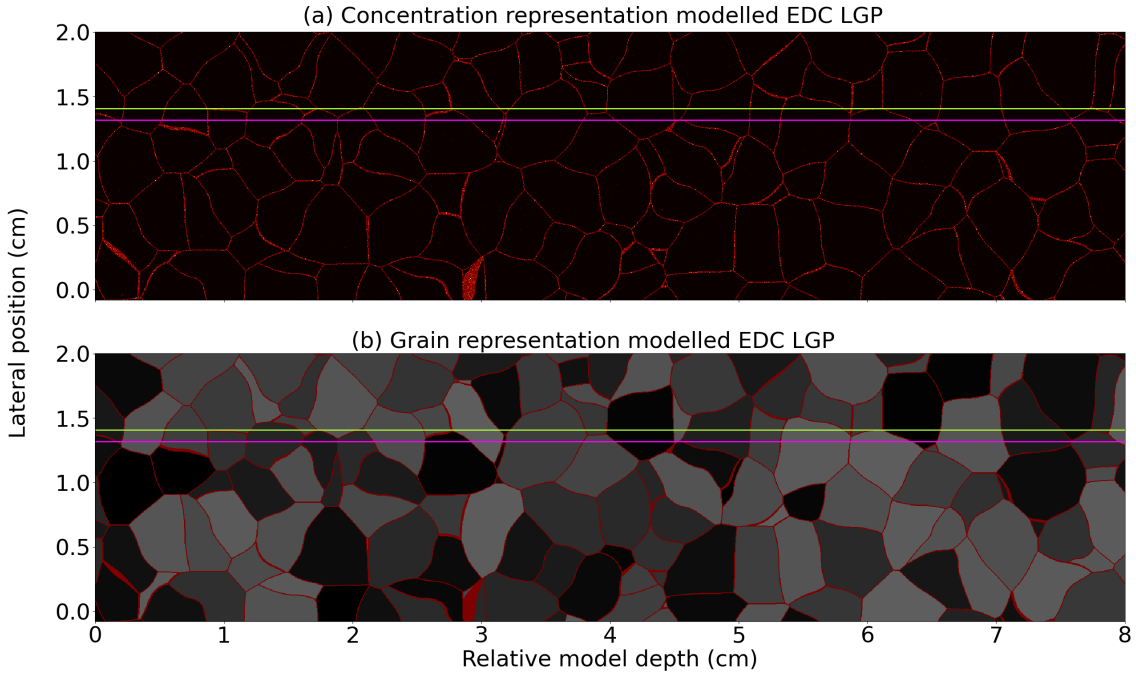

Figure S22. Plots equivalent to Fig. S2 showing the modelled data for the calibrated EDC LGP dataset.

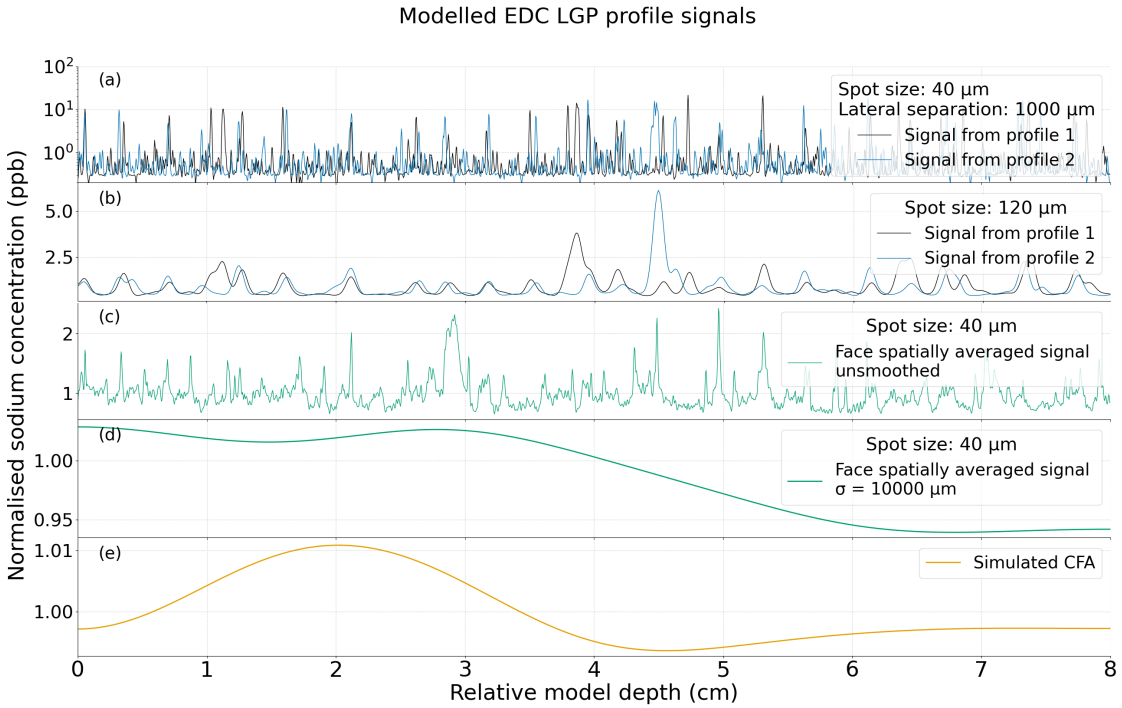

Figure S23. Plots equivalent to Fig. S3 showing the two profiles plotted in Fig. S22 for modelled calibrated EDC LGP data.

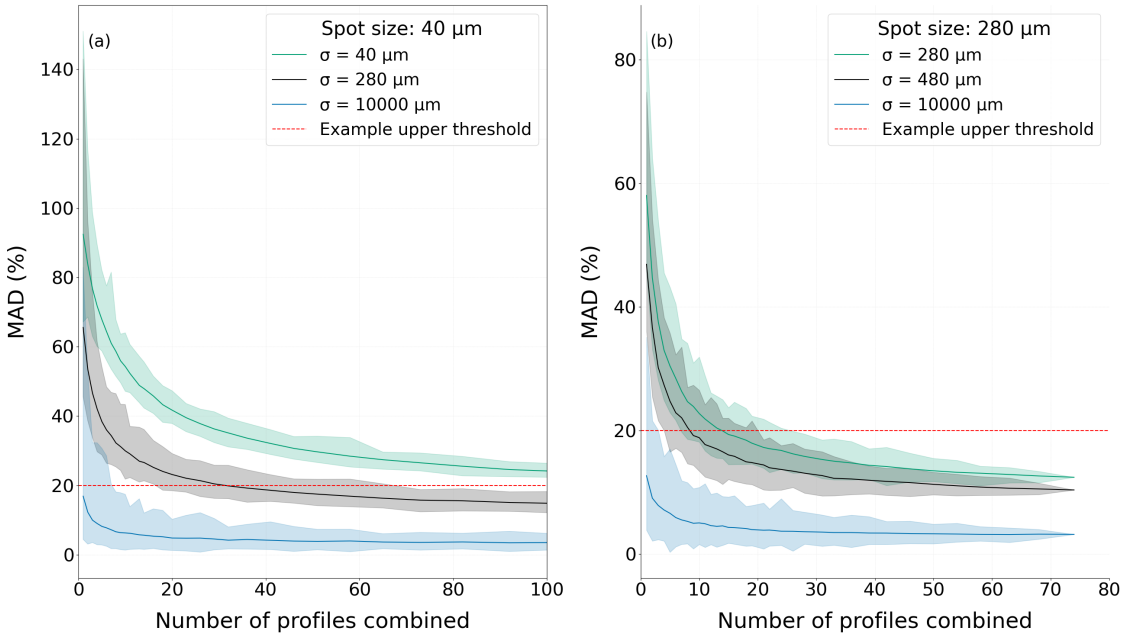

Figure S24. Plots equivalent to Fig. S4 for modelled calibrated EDC LGP data.

References

Binder, T., Garbe, C., Wagenbach, D., Freitag, J., and Kipfstuhl, S.: Extraction and parametrization of grain boundary networks in glacier ice, using a dedicated method of automatic image analysis, J. Microsc., 250, 130–141, https://doi.org/doi.org/10.1111/jmi.12029, 2013.

Bohleber, P., Larkman, P., Stoll, N., Clases, D., Gonzalez de Vega, R., Šala, M., Roman, M., and Barbante, C.: Quantitative insights on impurities in ice cores at the micro-scale from calibrated LA-ICP-MS imaging, Geochem. Geophys. Geosyst., 25, https://doi.org/doi.org/10.1029/2023GC011425, 2024.

Ferenc, J.-S. and Néda, S.: On the size distribution of Poisson Voronoi cells, Physica A: Statistical Mechanics and its Applications, 385, 518–526, https://doi.org/doi.org/10.1016/j.physa.2007.07.063, 2007.

Quey, R., Dawson, P., and Barbe, F.: Large-scale 3D random polycrystals for the finite element method: Generation, meshing and remeshing, Computer Methods in Applied Mechanics and Engineering, 200, 1729–1745, https://doi.org/doi.org/10.1016/j.cma.2011.01.002, 2011.